Magnetic properties of the zigzag ladder compound $SrTb_2O_4$

F. Orlandi,[1] M. Ciomaga Hatnean,[2,*] D. A. Mayoh,[2] J. P. Tidey,[3] S. X. M. Riberolles,[2] G. Balakrishnan,[2] P. Manuel,[1] D. D. Khalyavin,[1] H. C. Walker,[1] M. D. Le,[1] B. Ouladdiaf,[4] A. R. Wildes,[4] N. Qureshi,[4] and O. A. Petrenko[2,†]

[1]*ISIS Neutron and Muon Source, STFC Rutherford Appleton Laboratory, Chilton, Didcot OX11 0QX, United Kingdom*
[2]*Department of Physics, University of Warwick, Coventry CV4 7AL, United Kingdom*
[3]*Department of Chemistry, University of Warwick, Coventry CV4 7AL, United Kingdom*
[4]*Institut Laue-Langevin, 71 Avenue des Martyrs, CS 20156, 38042 Grenoble Cedex 9, France*

(Received 24 April 2024; revised 17 January 2025; accepted 21 January 2025; published 10 February 2025)

We report on the properties of $SrTb_2O_4$, a frustrated zigzag ladder antiferromagnet, studied by single crystal neutron diffraction (with polarized neutrons in zero field and unpolarized neutrons in an applied magnetic field), as well as by neutron spectroscopy on a polycrystalline sample. The neutron scattering results are supported by single-crystal magnetization and heat capacity measurements. In zero field, neutron diffraction data show no transition to a magnetically ordered state down to the lowest experimentally available temperature of 35 mK, and the material remains magnetically disordered down to this temperature. Polarized neutron diffraction measurements reveal the presence of a diffuse scattering signal suggesting only very weak spin-spin correlations in the ground state. For $H \parallel c$ (the easy magnetization direction), we followed the magnetization process using neutron diffraction measurements and observed the appearance of field-induced magnetic Bragg peaks with integer h and k indices in the $(hk0)$ scattering plane. No magnetic peaks with a nonzero propagation vector were detected. The observed in-field data fit well to a simple two-sublattice model with magnetic moments aligned along the field direction but being significantly different in magnitude for the two inequivalent Tb^{3+} sites in the unit cell. Overall, the collected data point to a nonmagnetic ground state in $SrTb_2O_4$ despite the presence of strong interactions.

DOI: 10.1103/PhysRevB.111.054415

I. INTRODUCTION

$SrTb_2O_4$ is a member of a large family of the $SrRE_2O_4$ oxides, where RE is a rare-earth atom [1–3]. The $SrRE_2O_4$ magnets demonstrate rather interesting properties mostly originating from their crystal structure (space group *Pnam*) which for magnetic ions consist of triangular zigzag ladders, as depicted in Fig. 1. Due to the resulting geometrical frustration, the ordering temperatures T_N for most family members are significantly lower than their Weiss temperatures, Θ_{CW}. In many cases the magnetic order is incomplete, and the range of the spin correlations remains limited even at the lowest temperatures, although it might extend over several unit cell lengths. Another factor influencing the unconventional behavior of the $SrRE_2O_4$ magnets is the presence of two different crystallographic positions for the RE ions in the orthorhombic unit cell (in $SrTb_2O_4$, they are labeled as Tb1 and Tb2 in Fig. 1). Despite rather similar crystallographic arrangements for the RE ions in the two positions, with only marginally more distorted oxygen octahedra surrounding one of them, they usually demonstrate very different magnetic behavior [4–7].

The magnetic properties of the RE containing materials are often governed by spin anisotropy which in turn is determined by crystal electric field (CEF) effects. Ising-like, XY-like, and Heisenberg-like behaviours are all found in different $SrRE_2O_4$ magnets. When studying the families of the RE containing compounds which share the same chemical composition and crystal symmetry, but contain different RE elements, a better understanding of the magnetic properties of the entire family can be achieved by comparing and contrasting the CEF level schemes of the individual compounds. The behavior of the magnets containing Tb^{3+} ions ($S = L = 3, J = 6$) is often special in this respect, as singlet or nonmagnetic ground states are frequently found. This possibility makes studies of the Tb^{3+} containing materials both challenging and exciting, $Tb_2Ti_2O_7$ is a good example of a magnetic system which required more than two decades of concerted efforts [8–11] to tackle what is considered to be an "ongoing conundrum" in the study of RE pyrochlores.

To properly place $SrTb_2O_4$ among other $SrRE_2O_4$ family members, we briefly list here their magnetic properties. $SrEr_2O_4$ undergoes a transition at 0.75 K [12] with magnetic moments on the Er1 site forming a fully ordered $\mathbf{q} = 0$

*Present address: Laboratory for Multiscale materials eXperiments, Paul Scherrer Institute, 5232 Villigen PSI, Switzerland; Materials Discovery Laboratory, Department of Materials, ETH Zurich, 8093 Zurich, Switzerland.
†Contact author: o.petrenko@warwick.ac.uk

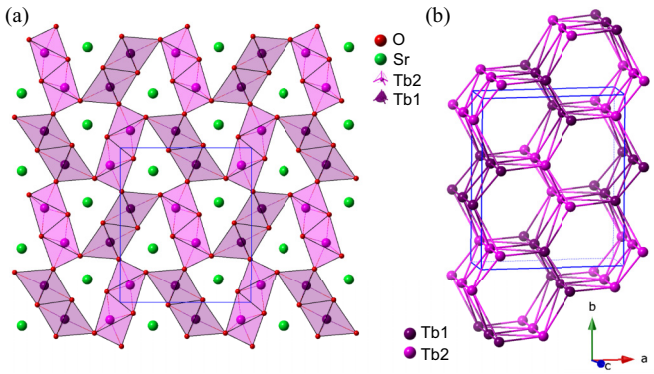

FIG. 1. (a) Crystal structure of $SrTb_2O_4$ projected onto the *a*-*b* plane. Different colours used for the oxygen octahedra hosting the Tb ions emphasize the presence of two inequivalent crystallographic positions, labeled Tb1 and Tb2. (b) The zigzag ladders formed by the Tb1 and Tb2 magnetic ions and their arrangement into a distorted honeycomb lattice in $SrTb_2O_4$. The unit cell is indicated by the solid blue lines for panels (a) and (b).

antiferromagnet, while the magnetic moments on the Er2 site form a collection of weakly correlated antiferromagnetic chains with only a short-range order described by a $\mathbf{q} = (00q_z)$ propagation vector with $q_z \approx 0.5$ [4]. A similar coexistence of two types of magnetic order is also found in $SrHo_2O_4$, but in this compound even the $\mathbf{q} = 0$ structure remains short-ranged down to the lowest temperatures despite a pronounced increase in the magnetic correlations below 0.7 K [5]. Long-range order in $SrDy_2O_4$ is absent down to the mK range [13–15]. $SrYb_2O_4$ orders at 0.9 K to a noncollinear structure with a reduced moment on both Yb sites [16]. $SrNd_2O_4$ orders at 2.28 K with only one Nd site carrying a significant magnetic moment [17]. $SrGd_2O_4$ shows an initial transition at 2.73 K to a commensurate antiferromagnetic structure and then a further transition at 0.48 K to an incommensurate structure with $\mathbf{q} = (0\,0\,0.42)$ where both Gd sites are long-range ordered [18].

In an applied magnetic field, all the $SrRE_2O_4$ compounds demonstrate highly anisotropic behavior often forming rather complex, partially ordered states. The in-field ground states of $SrEr_2O_4$, $SrHo_2O_4$, $SrDy_2O_4$, and perhaps other $SrRE_2O_4$ family members could adequately be described by an Ising model on a honeycomb zigzag-ladder lattice with two different types of magnetic sites [19].

Given the above, the reported magnetic properties of $SrTb_2O_4$ [20] are surprising from at least two perspectives. The first one is the highest ordering temperature of 4.28 K [20] in the whole family. The second is the observed incommensurate magnetic structure with a propagation vector of $\mathbf{q} \approx (0.5924\,0.0059\,0)$ [20], implying ferromagnetic ordering along the *c* axis and an incommensurate modulation along the *a* and *b* axes. It is difficult to understand what combination of the magnetic coupling constants, either of exchange or the dipole-dipole origin, could potentially cause such an arrangement. None of the other family members have a similar propagation vector. For all of the studied $SrRE_2O_4$ compounds, the a^* component of the propagation vector q_x is zero. In fact, the only example of the ordering with a nonzero q_x is reported for $BaDy_2O_4$ [21], a member of the $BaRE_2O_4$ family with an identical crystal structure [22]. However, in $BaDy_2O_4$ the two propagation vectors, $\mathbf{q}_1 = (\frac{1}{2}0\frac{1}{2})$ and $\mathbf{q}_2 = (\frac{1}{2}\frac{1}{2}\frac{1}{2})$ both have nonzero c^* components, q_z, indicating an antiferromagnetic arrangement along the *c* axis, which makes the magnetic structure much more "rational"—an increase of the unit cell along only the *a* axis, without altering the arrangements within the zigzag ladders running along the *c* axis, is unlikely to relieve the geometrical frustration.

Notably, the Tb^{3+} compound $BaTb_2O_4$ from the same $BaRE_2O_4$ family is found to be in a cooperative paramagnetic or spin-liquid ground state down to 95 mK [23].

In this paper we report the preparation of high-quality single-crystal samples of $SrTb_2O_4$ and a detailed investigation of their magnetic properties. In zero field, the samples remain in a magnetically disordered state down to at least 35 mK. The whole volume of the collected data is consistent with a picture of a magnetically disordered ground state and a field-induced magnetic polarization of the magnetic Tb^{3+} ions.

II. SAMPLE PREPARATION AND EXPERIMENTAL DETAILS

A polycrystalline sample of $SrTb_2O_4$ was prepared by grinding together stoichiometric $SrCO_3$ (99.999%, Strem Chemicals) and Tb_4O_7 (99.9%, Strem Chemicals) with an excess of 12.5% $SrCO_3$ to compensate for the loss of Sr during the synthesis. The resulting ground powder was pressed into pellets of approximately 2 g each. The pellets were then sintered in an argon-hydrogen (Ar + 2% H_2) atmosphere at 900 and 1450 °C for 12 and 48 hours respectively, with intermediate regrinding and repressing. The samples prepared contained a few percent of Tb_2O_3 and SrO_2 impurities.

A single crystal of $SrTb_2O_4$ was grown using the optical floating-zone technique (an image of the crystal boule is given in Fig. S1 in the Supplemental Material [24]). Polycrystalline rods were used for both the feed and seed rods for the crystal growth. The crystal growth was carried out in a high purity (99.9999%) argon gas pressure of about 1 bar and at a growth rate of 3–5 mm/h.

Powder x-ray diffraction was performed using Panalytical X-Pert Pro MPD which has a Cu x-ray source equipped with a focusing Johansson monochromator to the incident optics to give monochromatic $K_{\alpha 1}$ radiation ($\lambda = 1.5406$ Å).

Single-crystal x-ray diffraction data for $SrTb_2O_4$ were collected for a crystal of dimension $0.04 \times 0.06 \times 0.13$ mm^3 using a Rigaku Oxford Diffraction Synergy S equipped with a HyPix-6000HE Hybrid Photon Counting detector and employing mirror monochromated Mo K_α radiation ($\lambda = 0.71073$ Å) source. The temperature of the crystal was controlled using an Oxford Cryosystems Cryostream at 300 K. CrysAlisPRO was used for the data collection, indexing, reduction, and absorption corrections [25]. A structural solution was obtained using SHELXT [26] and further refined by full-matrix least squares using SHELXL [27], both operating through OLEX2 [28].

High crystallinity of the grown crystal was confirmed by x-ray and neutron Laue diffraction techniques. A single-crystal sample, $m \approx 120$ mg, was used for the zero-field Laue diffraction measurements on CYCLOPS [29] and polarized

neutron diffraction measurements on D7 [30] at the Institut Laue-Langevin (Grenoble, France) as well as for the in-field measurements on the WISH time-of-flight instrument [31] at ISIS (STFC Rutherford Appleton Laboratory, United Kingdom).

CYCLOPS is a very large solid-angle Laue neutron diffractometer using CCD detector with a very fast read-out system allowing real-time Laue diffraction experiments [29]. An orange cryostat has been used to cover the temperature range 2 to 10 K in the experiment. A set of Laue patterns has been collected at different omega angles to access a large volume of reciprocal space especially at low scattering angles relevant for magnetic reflections.

The magnetic correlations were probed using D7, the diffuse scattering spectrometer with polarization analysis [32]. The single-crystal sample was mounted on an aluminium pin, and the pin was masked with cadmium. The horizontal ($hk0$) plane was explored by rotating the sample around the vertical c axis in 1° steps, two different positions of the detectors allowed for a denser coverage of the reciprocal space. The incident neutrons wavelength was $\lambda = 3.1$ Å. During the experiment, the neutron polarization was normal to the scattering plane and non-spin-flip (NSF) and spin-flip (SF) datasets were collected. A standard orange cryostat provided a base temperature of 1.5 K, and the instrument background was estimated by measuring the empty cryostat.

Unpolarized single-crystal measurements were performed as a function of applied magnetic field on WISH [33]. A dilution refrigerator with base temperature of 35 mK was used in combination with a 10 T cryomagnet. An oxygen-free copper sample holder provided good thermal link from the mixing chamber to the sample. The vertical magnetic field was applied along the c axis; this setup provided access to the horizontal ($hk0$) scattering plane. We used three different sample positions to maximize neutron flux for different portions of reciprocal space and to collect the intensity of a large number of magnetic and nuclear peaks. Typical measurement time for a single position was 30 minutes. The integration of the diffracted peaks at 0 and 80 kOe was performed with the MANTID software [34]. The data were corrected for incident flux, Lorentz factor and detector efficiency. The integration has been performed in Q space using an elliptical region of interest on predicted peaks position. The main axes of the ellipse for each reflection were determined from the estimated covariance of the data. The refinements were performed with the help of the Jana2006 software [35] and group theoretical calculations were performed with the ISOTROPY suite of software [36].

Inelastic neutron scattering experiments were performed using 2.6 g of polycrystalline $SrTb_2O_4$ on the MERLIN direct geometry chopper spectrometer [37] at the ISIS neutron and muon facility. The sample was wrapped in aluminium foil to form an annulus and inserted into a closed-cycle refrigerator in a cylindrical aluminium can. Two chopper configurations were used to give focused incident energies of 7 and 30 meV at frequencies of 150 and 300 Hz, respectively. Each configuration also yielded additional "reps" at 18 meV (150 Hz setting) and 80 meV (300 Hz setting) using repetition-rate multiplication method. The raw data [38] were processed using the MANTID software package [34] following the standard conventions.

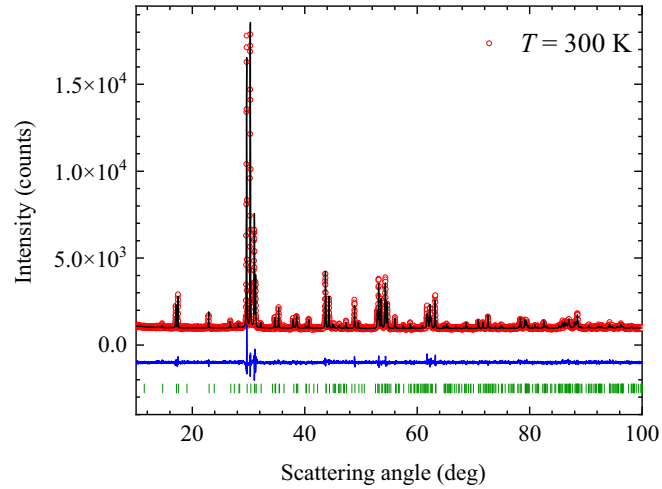

FIG. 2. Refinement of the powder x-ray diffraction profile of the ground crystal of $SrTb_2O_4$ measured at room temperature using a Cu x-ray source. Data, fit, and their difference are displayed in red, black, and blue, respectively. The positions of the nuclear reflections allowed within the *Pnam* crystal structure of $SrTb_2O_4$ are indicated by vertical green bars.

Magnetisation measurements were performed on both single-crystal and polycrystalline samples of $SrTb_2O_4$ using a Quantum Design Magnetic Property Measurement System (MPMS) magnetometer as well as an Oxford Instruments vibrating-sample magnetometer (VSM). Specific heat was measured on single-crystal samples by the standard 2τ method using a Quantum Design Physical Property Measurement System (PPMS) calorimeter in the temperature range 1.8–50 K in applied fields of 0, 20, 40, 60, and 80 kOe. The zero-field data collection was extended down to 0.6 K by using a ^{3}He option.

III. RESULTS, ANALYSIS AND DISCUSSION

A. Powder and single-crystal x-ray diffraction

Powder x-ray diffraction patterns taken on ground crystals of $SrTb_2O_4$ revealed their high chemical purity (see Fig. 2), with no detectable impurity peaks. Therefore, the powder sample used on MERLIN was prepared by grinding the grown crystals. A record of the crystal structure parameters determined from XRD pattern refinement is summarized in Table I. The crystal structure parameters are similar to those reported in Ref. [20].

Single-crystal x-ray diffraction was used to further confirm the structure of the single crystals of $SrTb_2O_4$ grown by the floating zone technique. The structural parameters derived from the single-crystal x-ray diffraction data are listed in Table I, and a cif file containing all the information is provided as Supplemental Material [24]. It is also worth underlining the good agreement between the powder and single-crystal refinement indicating high sample quality and the lack of strain or inhomogeneities in the samples.

TABLE I. Crystal data, reliability factors and structural parameters resulting from the single-crystal and powder x-ray diffraction experiments. The space group is *Pnam*, the atomic positions are all at the 4c Wyckoff site $(x, y, 1/4)$. For the Powder XRD, the isotropic atomic displacement parameter B_{iso} was fixed to 0.97 Å^2 for all atoms, whereas for the single-crystal data atomic displacement parameters were refined independently for each site and are reported in the cif file provided as Supplemental Material [24].

Technique	Single-crystal XRD	Powder XRD
a (Å)	10.0827(2)	10.10385(8)
b (Å)	11.9876(4)	12.00133(9)
c (Å)	3.4506(1)	3.45324(4)
R_1 (%)	1.79	
wR_2 (%)	4.4	
R_{wp}		4.474
R_{exp}		3.307
R_{Bragg}		1.189
GoF (%)	1.325	1.496
Sr x, y	0.75073(3) 0.64866(3)	0.7510(4) 0.6492(3)
O1 x, y	0.2142(3) 0.1801(2)	0.220(3) 0.1822(16)
O2 x, y	0.1291(3) 0.4825(2)	0.127(2) 0.4926(19)
O3 x, y	0.5099(3) 0.7846(2)	0.481(3) 0.7792(15)
O4 x, y	0.4265(3) 0.4214(2)	0.418(4) 0.4064(16)
Tb1 x, y	0.42484(2) 0.11191(2)	0.4232(4) 0.1122(2)
Tb2 x, y	0.41883(2) 0.61157(2)	0.4199(4) 0.6111(2)

B. Inelastic neutron scattering

Inelastic neutron scattering (INS) spectra measured on the time-of-flight MERLIN spectrometer at ISIS are shown in Fig. 3. Spectra with incident neutrons of 18 and 30 meV were found to be very similar so for brevity we show only the 18 meV data. The latter data, measured at $T = 7$ K, revealed the presence of three well-defined CEF excitations at 7.6, 11.4, and 12.7 meV (the higher-energy branches are slightly overlapping). The excitations are largely nondispersive, although there is a visible modulation of the intensity of the 7.6 meV branch with increasing scattering vector Q.

The lower-energy excitations observed with incident neutrons of 7 meV demonstrate a significantly more complex behavior. There are two strong, nearly flat excitation branches at 0.71 and 1.42 meV whose intensity is maximum around $Q \approx 1.25$ Å^{-1}. The third, much weaker excitation branch at 2.22 meV appears to be strongly dispersive with an energy minimum at the same Q.

The measurements with the highest energy neutrons of 82 meV (shown in Fig. S2 in the Supplemental Material [24]) revealed the presence of two further partially overlapping CEF excitations at 27.3 and 31.1 meV. There are no visible CEF levels above these energies all the way up to at least 70 meV, with the excitation spectrum at higher scattering vector, $Q > 6$ Å^{-1} being dominated by the phonons.

The temperature evolution of the CEF energy spectrum is shown in Fig. S3 in the Supplemental Material [24].

These results indicate a potential influence of exchange interactions on the CEF excitations, although the strength of the exchange coupling appears to be insufficient to drive the system into a magnetically ordered state, so it remains in a disordered (correlated paramagnetic) phase [39,40].

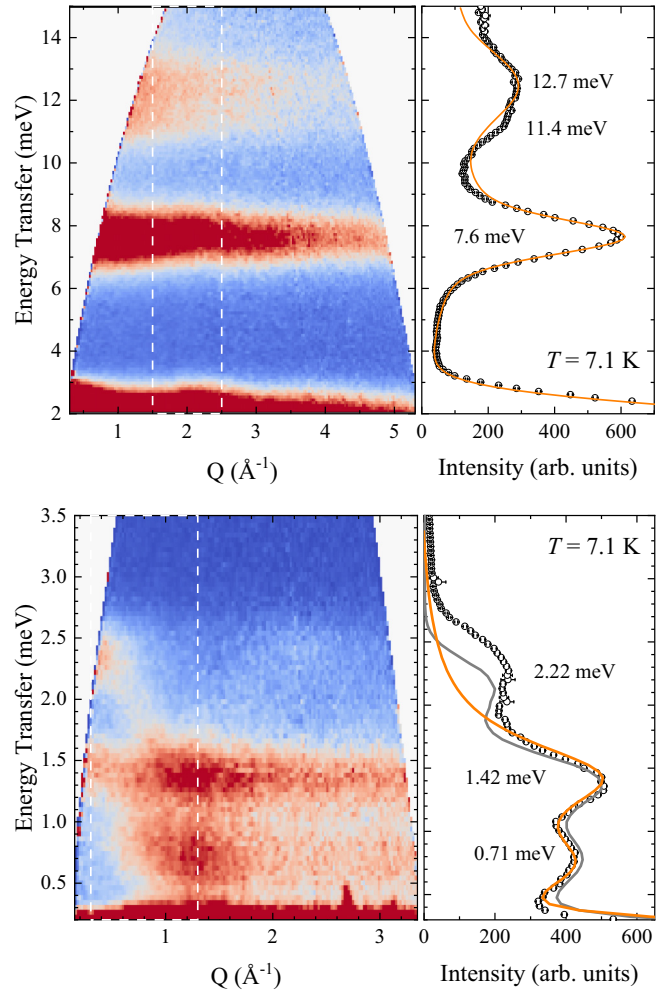

FIG. 3. INS spectra of $SrTb_2O_4$ powder sample measured on MERLIN at $T = 7.1$ K with different energy neutrons (top) $E_i = 18$ meV and (bottom) $E_i = 7$ meV. To identify the exact energies of the observed excitations, the cuts along the energy transfer are shown to the right of the color intensity maps. White dashed lines on the color maps indicate the area used for the cuts. The experimental data (black symbols) were fit as Gaussians and a linear background, with the peak centres shown near each peak. The calculated spectra from parameters in Table II are shown in both panels by the solid orange lines. In the lower panel, the grey line shows the calculated spectrum using the mean-field random-phase approximation.

In addition to being responsible for the dispersion of the 2.22 meV mode, the exchange interaction broadens the linewidths of the CEF excitations and makes it more difficult to distinguish if there are multiple nearby peaks. Furthermore, while the RE sites in the $SrRE_2O_4$ compounds have monoclinic point symmetry $C_s(m)$, which leads to the splitting of the $J = 6$ multiplet into the maximum number of levels ($2J + 1 = 13$ singlets). However, the local environment is close enough to hexagonal that several quasi-doublet pairs could be expected to be found.

Although attempts have been made to compute the CEF levels in the past for $SrDy_2O_4$ and $SrHo_2O_4$ [2] as well as more recently for $SrTm_2O_4$ [41], the large number of parameters (caused by the presence of the two inequivalent sites) and

TABLE II. Crystal field parameters $B_p^q = A_p^q \langle r^p \rangle \theta_p$ (in meV) for the Tb^{3+} ions at two crystallographic sites, Tb1 and Tb2, as determined from fitting the inelastic neutron scattering data.

	Tb1	Tb2
B_0^2	−0.17741	0.055311
B_2^2	−0.094645	0.75653
B_{-2}^2	2.9595×10^{-6}	-5.9839×10^{-5}
B_0^4	−0.0074249	0.020207
B_2^4	−0.0025211	0.0074979
B_{-2}^4	-1.372×10^{-5}	4.9393×10^{-6}
B_4^4	1.5492×10^{-5}	4.0977×10^{-6}
B_{-4}^4	−0.00011748	2.6124×10^{-5}
B_0^6	-7.3581×10^{-5}	1.5577×10^{-5}
B_2^6	0.2401	0.24772
B_{-2}^6	0.013588	−0.017102
B_4^6	−0.011204	−0.012231
B_{-4}^6	-1.1458×10^{-5}	3.3862×10^{-5}
B_6^6	0.00013938	-7.4905×10^{-5}
B_{-6}^6	6.7939×10^{-5}	3.6555×10^{-5}

the relatively small number of observed CEF levels make such computations prone to significant uncertainties.

Despite these difficulties, using a constrained fitting procedure we were able to find a set of CEF parameters consistent with the INS spectra and which yielded qualitative agreement with the observed magnetization and susceptibility behavior. We should note that these are only one of several nearly equivalent CEF parameter sets, albeit the one with the lowest χ^2 statistic.

In all cases we found that we cannot fit three low energy excitations. In order to fit the intermediate (at 7–13 meV) and high energy (≈30 meV) excitations, and to maintain qualitative agreement with the measured magnetic susceptibility and magnetization, we found that only schemes with one low energy (<5 meV) excitation per Tb site satisfied the data. As such, we assigned the 0.71 and 1.42 meV levels as "true" CEF levels while the 2.22 meV excitation is deemed to be a dispersive exciton which originates from the same site together with the 0.71 meV mode, as indicated by the lack of intensity at low Q around 0.71 meV.

As each Tb1 (Tb2) ion is coupled to another Tb1 (Tb2) ion in the same unit cell by two different exchange interactions, it is possible to split the same singlet single-ion level into two modes, even in the absence of magnetic ordering, as was observed for the hexagonal U2 sites in UPd_3 [42]. The lack of dispersion of the 1.42 meV mode thus indicates that the exchange interaction between ions on one site is stronger than between ions on the other site. Despite this hint, however, in order to properly fit the data we should also include the inter-site exchange coupling, which yields a minimum model of five exchange interactions (two intrasite couplings for each site and the intersite coupling). Our powder neutron data, unfortunately, are not sufficient to fit such a model, which is the proper subject of future work requiring either single-crystal INS measurements of the low-energy modes, or a detailed *ab initio* calculation of the exchange interactions. Thus in the following we fit only the single-ion crystal-field parameters. However, we found that after fitting the CEF parameters we were able to use a phenomenological model of the exchange to account for the 2.2 meV peak, although it does not fully match the data.

In order to constrain the fit, each iteration was divided into two steps: (1) the input CEF parameters is first refined with respect to the measured energy levels of 0.71, 7.64, and 27.3 meV (Tb1 site), and 1.42, 12.7, and 31.1 meV (Tb2 site) with the wave functions (eigenvectors) as variational parameters in an algorithm first proposed by Newman and Ng [43]. The assignment of the energy levels between the two sites was done on the basis of initial parameters from the literature [44,45] and trial and error. Energy levels not determined from experimental data were left unchanged in the variational procedure. (2) The peak positions and intensities were calculated from the refined CEF parameters in step 1, and a fit of the peak widths was completed yielding a summed χ^2 statistic for the three cuts to the data (the two shown in Fig. 3 and that in Fig. S2 in the Supplemental Material [24]). Finally, a penalty was added to the χ^2 value based on the differences between the measured susceptibility values at 300 K and magnetization at 80 kOe and those calculated using the CEF parameters. This combined INS χ^2 and physical properties penalty function was then minimized using both local and global search algorithms.

The two-step iteration ensured that only the CEF parameters themselves are varied between iterations. The first step also constrains the energy levels to be close to that measured, while the second step means that the peak widths (which are not resolution limited due to the exchange interaction) should not affect the fitting of the CEF parameters.

Starting from the CEF parameters in the literature [44–46], we then refined the B_0^2 and B_0^4 parameters on each site by trial and error to obtain energy level and intensity schemes which resemble the data. We then perform a local minimization using Powell's method as implemented in the Scipy Optimize package [47] to find the parameters in Table II, yielding the energy levels in Table III. In addition, we also explored using a global search with the "differential evolution" algorithm as implemented in Scipy to find other starting parameters which were subsequently fitted using Powell's method but did not find a significantly better set of CEF parameters. We used the MANTID [34,48] program for the crystal-field calculations and the full source code is available for download [49].

The above procedure, and indeed the INS data themselves, can only yield two sets of CEF parameters corresponding to the different Tb sites but cannot explicitly say that a

TABLE III. Energy levels from the crystal-field parameters in Table II in meV.

0	0.74	7.63	8.95	17.19	28.39	29.32	43.45	45.18	50.64	50.87	54.90	56.96
0	1.43	12.46	15.23	27.29	30.22	45.95	63.24	63.66	80.19	84.84	89.02	91.98

particular set corresponds to a particular site. We have made the assignments in Table II based on fitting a point charge model with the Tb1 and Tb2 sites in the positions noted in Table I. This assignment yielded the lowest mean absolute error (MAE $= \frac{1}{n}\sum_{p,q}|V_q^p(\text{pc}) - V_q^p(\text{INS})|$ where n is the number of parameters) of 0.32 meV between the normalized point charge model calculated parameters and the normalized INS fitted parameters. V_q^p denote the "normalized" crystal-field parameters defined by Fabi [50]. However, we note that the reverse assignment yielded only a slightly worse MAE of 0.34 meV but required large negative effective point charges for the metallic ions which we believe is physically implausible despite the limitations of the point charge model. More plausible point charge models yielded larger MAE around 0.45 meV.

With the parameter assignments in Table II, we found that the calculated magnetic moment for an 80 kOe field along the c direction is 7.3 μ_B/Tb for Tb1 and 1.6 μ_B/Tb for Tb2 which is in reasonable agreement with the diffraction results in Sec. III D 3.

Finally, we mentioned above that we assigned the 2.2 meV peak to a dispersive exciton. Using the fitted CEF parameters, and a phenomenological model of the (Heisenberg) exchange, $J(r) = A\cos(2kr)/(2kr)^3$ where r is the distance between pairs of ions and $A = 0.4$ meV, $k = 0.5$ Å^{-1}, we found that a mean-field random-phase approximation calculation using the MCPHASE [51] program could explain the 2.2 meV peak and fit the cut, as shown in Fig. 3. We also attempted to use a simpler model, $J(r) = A/r^n$ but this could not fit the data, indicating that there is some complexity between the exchange interactions which likely requires single-crystal data to unravel.

A more robust approach to the determination of the CEF parameters is through a combination of the INS data with the site-selective optical and EPR measurements performed on samples of a nonmagnetic analog, such as SrY_2O_4 for example, with a small amount of substitution of the magnetic rare earth ion. Such an approach was used for $SrEr_2O_4$ [44] and SrY_2O_4:Er^{3+}, where the sets of parameters was derived which fitted all the available experimental data well, including the magnetization and susceptibility data for dilute and concentrated samples.

According to the latest EPR results [45], for Tb1 sites the nonzero component of the g-factor is along the c axis, and the energy levels splitting is similar to what was previously obtained for Er1, Dy1, and Ho1 sites. The situation is, however, less clear with the Tb2 sites (the easy-axis direction is near the b axis for them), as the observed optical spectra are inconsistent with the sets of crystal-field parameters used for other members of the family [45].

The crystal-field parameters obtained from fitting the $SrTb_2O_4$ INS data is generally in agreement with the optical spectroscopy and EPR results obtained for dilute SrY_2O_4:Dy^{3+}, SrY_2O_4:Ho^{3+}, and for $SrEr_2O_4$ (see Table I in the Supplemental Material [24]). However, there are some notable differences, particularly for the $B^6_{\pm4}$ parameters which are an order of magnitude larger in the INS fit compared with those obtained from optical spectra. These parameters, though, are crucial to obtain the very low energy levels at 0.71 and 1.42 meV. With lower values of $B^6_{\pm4}$, the splitting between the ground state and the first excited state becomes significantly larger (≈ 2 meV for an order of magnitude reduction in $B^6_{\pm4}$).

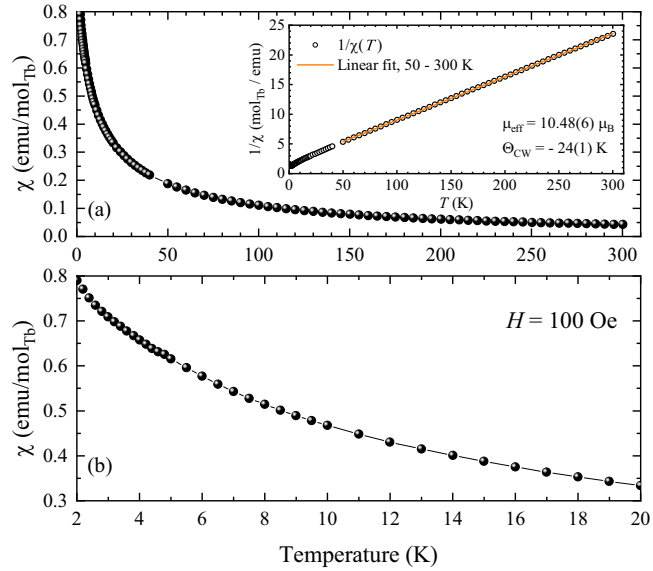

FIG. 4. Temperature dependence of the magnetic susceptibility, $\chi(T)$, measured on a powder sample of $SrTb_2O_4$ in an applied field of 100 Oe. Panel (a) shows the entire T range covered, 2 to 300 K, while panel (b) focuses on the low-T behavior, emphasizing the absence of any discernible features in the range 2 to 20 K. The inset shows a Curie-Weiss fit to the inverse susceptibility.

C. Magnetization and heat capacity measurements

Figure 4 shows the temperature dependence of the magnetic susceptibility $\chi(T)$ of a polycrystalline sample of $SrTb_2O_4$. At higher temperatures, the susceptibility follows the Curie-Weiss law, a linear fit in the range 50 to 300 K reveals $\Theta_{CW} = -24(1)$ K and slightly larger than expected value of the effective magnetic moment of $\mu_{eff} = 10.48(6)\mu_B$ per Tb^{3+} ion. This could potentially be explained by the presence of a small frozen field in the superconducting magnet of the MPMS magnetometer (just 10 Oe of frozen field would be sufficient to bring the value of μ_{eff} below $10\mu_B$).

A previous publication [52] reported a significant deviation from the Curie-Weiss behavior below about 160 K and used a temperature range of 180 to 280 K to obtain $\Theta_{CW} = 5.00(4)$ K. The positive (ferromagnetic) sign of Θ_{CW} in $SrTb_2O_4$ would be very surprising given the fact that all seven $SrRE_2O_4$ family members for which $\chi(T)$ is known [1,17] have a negative Θ_{CW} ranging from about -10 to -100 K. We note that in Ref. [52], the susceptibility data were recorded for a "randomly oriented" $SrTb_2O_4$ crystal and, given the highly anisotropic nature of $\chi(T)$, determination of Θ_{CW} from such data is rather unreliable.

Figure 4(b) shows the low-temperature (2 to 20 K) behavior of $\chi(T)$ highlighting a rather smooth variation in the entire region shown, with no evidence for a phase transition around the suggested ordering temperature of 4.28 K [20].

The temperature dependence of the magnetic susceptibility measured on a single-crystal sample is given in Fig. 5(a). The susceptibility is highly anisotropic and is largest for $H \parallel c$. The

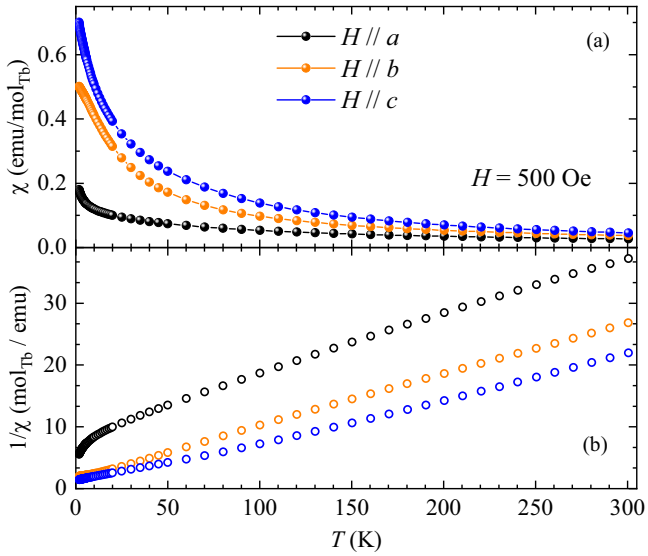

FIG. 5. Temperature dependence of (a) the magnetic susceptibility, $\chi(T)$ and (b) the inverse susceptibility, $1/\chi(T)$, measured on a single-crystal sample of $SrTb_2O_4$ in a field of 500 Oe applied along the three principal axes.

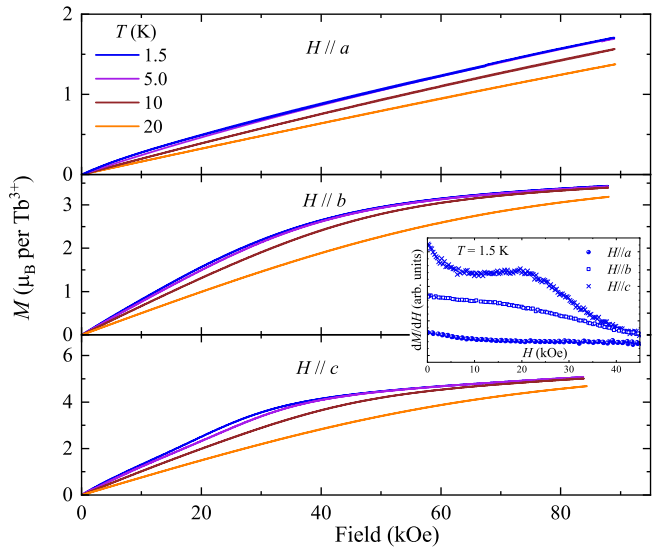

FIG. 6. Field dependence of magnetization $M(H)$ of $SrTb_2O_4$ single crystal measured at various temperatures for the three principal directions of the magnetic field H. The inset shows field derivatives $dM(H)/dH$ of magnetization measured at $T = 1.5$ K. The applied field is demagnetization-corrected.

inverse susceptibility [Fig. 5(b)] is not linear with temperature for any direction of an applied field; however, when averaged over the three directions, $1/\chi(T)$ does follow the Curie-Weiss law (see Fig. S4 in the Supplemental Material [24]). The nonlinearity of the inverse susceptibility as well as the highly anisotropic nature can be explained by the influence of the low-energy CEF levels observed in our INS data.

A linear fit of the averaged inverse susceptibility in the range 50 to 300 K gives a magnetic moment of $\mu_{\text{eff}} = 9.8(1)\mu_B$ per Tb^{3+} ion and $\Theta_{CW} = -44(1)$ K. Again, the low-temperature behavior of the $\chi(T)$ curves for all three directions of the applied field is rather smooth, giving no reason to suspect a magnetic ordering transition down to at least 2 K. We note that the recent susceptibility measurements [53] performed on the sample used in Ref. [20] returned results very similar to those shown in Fig. 4; that is, for the sample for which a magnetic ordering transition was suggested at 4.28 K, the magnetic susceptibility returns no signs of such a transition.

The field dependence of the magnetization measured on a single-crystal sample of $SrTb_2O_4$ for H parallel to the three principal crystallographic axes is shown in Fig. 6. For the purposes of calculating the demagnetization field, the sample was approximated to a rectangular prism with the length along the c axis half that of the other two directions. The field applied along the c axis returns the highest magnetization, while the a axis seems to be the hardest to magnetize along. There is no significant difference between the magnetization curves measured at 1.5 and 5.0 K for all three fields directions, again emphasizing the fact that no ordering occurs between these temperatures. Magnetization curves do not follow the Brillouin function expected for a simple paramagnet at any of the temperatures measured, but they are in qualitative agreement with the calculations based on the crystal-field parameters shown in Tables II and III.

At low temperatures, for $H \parallel c$, there is a broad maximum in the derivative $dM(H)/dH$ at around 20 kOe (clearly absent for $H \parallel a$ and $H \parallel b$), as shown in the inset in Fig. 6. A nonlinear field dependence of the derivative of magnetization $dM(H)/dH$ has also been observed for $SrEr_2O_4$, $SrDy_2O_4$, $SrHo_2O_4$, and $SrYb_2O_4$ single crystals [16,54,55] as well as powder samples [1] at temperatures well above the magnetic ordering in these compounds. Very often, the features in the $dM(H)/dH$ curves are amplified on further cooling, particularly below the magnetic ordering temperatures. They indicate the boundaries of the fractional magnetization plateaus (typically of the 1/3 type associated with the up-up-down structures) or the locations of the metamagnetic transitions. Given that $SrTb_2O_4$ remains in a magnetically disordered state down to the lowest temperature achieved in this study, it is not surprising that no well-defined magnetization plateaus are observed in this compound, which is dominated by the single-ion physics rather than by the exchange interactions.

A large influence of the crystal-field effects is also evident from the fact that only about a half of the full magnetic moment expected for the Tb^{3+} ions is recovered in the highest applied field of 90 kOe. This situation is fully consistent with our CEF calculations; it is also common for many members of the $SrRE_2O_4$ family, as the rare-earth ions at the two crystallographic sites often have nearly orthogonal directions for easy-axis magnetization, which makes full magnetic polarization nearly impossible for any field direction.

Figure 7 summarizes the results of the heat capacity measurements for the $SrTb_2O_4$ and the two nonmagnetic isostructural compounds, SrY_2O_4 and $SrLu_2O_4$. For all the compounds, the heat capacity is likely to reach the theoretical maximum, $7 \times 3R$ (seven being the number of atoms in the formula unit), well above room temperature. From

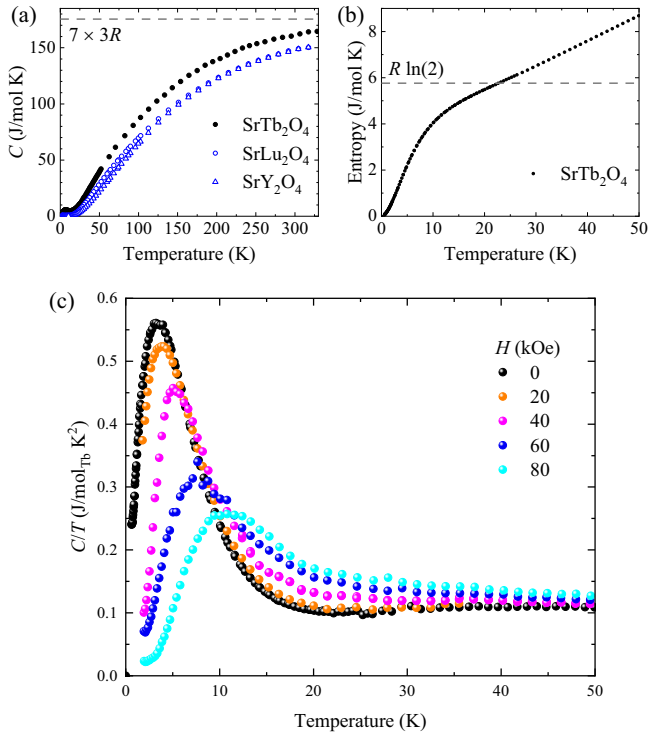

FIG. 7. (a) Temperature dependence of the heat capacity $C(T)$ of $SrTb_2O_4$ crystal as well as of the isostructural nonmagnetic SrY_2O_4 and $SrLu_2O_4$ compounds shown in the entire temperature range measured, 0.6 to 320 K. (b) Temperature dependence of the magnetic entropy of $SrTb_2O_4$ estimated from the $C_{mag}(T)/T$ curve after subtracting a phonon contribution. (c) $C_{mag}(T)/T$ curves (after subtracting the phonon contribution) measured in different fields applied along the c axis.

a direct comparison of the heat capacity curves, $C(T)$ [see Fig. 7(a)], it is rather obvious that $C(T)$ of $SrTb_2O_4$ is systematically higher than the heat capacity of the nonmagnetic blanks in the entire temperature range measured. The most likely reasons for that are the development of the magnetic correlations, particularly at the lower temperature, as well as the crystal-field effects, particularly at the intermediate and higher temperatures. Given the relatively small difference in $C(T)$ for SrY_2O_4 and $SrLu_2O_4$ and the fact that the Tb ions are much more similar in mass to the Lu ions compared with the Y ones, in all the calculations below we used the $SrLu_2O_4$ data for estimating the phonon contribution to the heat capacity of $SrTb_2O_4$.

Figure 7(b) shows the temperature dependence of the magnetic entropy of $SrTb_2O_4$ obtained by integrating the $C_{mag}(T)/T$ curves after the phonon contribution subtraction. Around $T \approx 22$ K the entropy exceeds the $R\ln(2)$ value expected for a simple model with an effective spin of 1/2 and increases further with increasing temperature.

Figure 7(c) demonstrates how the low-temperature part of the $C_{mag}(T)/T$ curves vary upon application of the magnetic field along the c axis. Although the maximum in $C_{mag}(T)/T$ curves remains clearly visible for all fields applied, it shifts to higher temperature with increasing field and also decreases in amplitude.

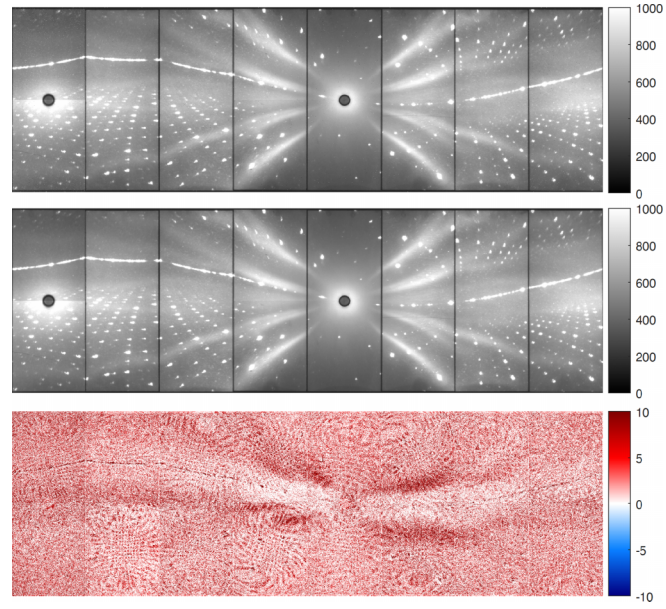

FIG. 8. Neutron Laue diffraction patterns of $SrTb_2O_4$ single crystal taken on the CYCLOPS diffractometer at the ILL at (top) 2.0 K and (middle) 10.0 K. The bottom panel is the digital difference between the two diffraction patterns shown above.

None of the curves, including the one measured at zero field, shows an anomaly at 4.28 K, providing further evidence for the absence of a magnetic transition at this temperature or, in fact, at any temperature down to at least 0.6 K (the lowest temperature reached in the heat capacity measurements).

D. Single-crystal neutron diffraction

1. Zero field Laue diffraction

The absence of magnetic ordering in $SrTb_2O_4$ is clearly seen from the neutron Laue diffraction patterns depicted in Figure 8 [56]. The two patterns taken at 2 and 10 K are identical, as seen in the difference plot (bottom panel of Fig. 8), and no extra peaks are detected at lower temperature, the intensities of all the Bragg peaks remain constant. All the peaks at both 10 and 2 K could be indexed within the nuclear *Pnam* group. To make sure that no extra magnetic peaks were missed, we repeated the measurements for a different sample orientation. The Laue patterns measured at 2 and 10 K (shown in Fig. S5 in the Supplemental Material [24]) were also identical in this case. Combining these observations with an exceptionally large coverage of the reciprocal space available on the CYCLOPS diffractometer [29], one can exclude the presence of any magnetic order with a nonzero propagation vector in $SrTb_2O_4$ down to at least $T = 2.0$ K.

We note that the powder neutron diffraction pattern reported in Ref. [20] contains just a single magnetic Bragg peak at 50 mK, and the intensity of this peak is rather weak, about 40% of the intensity of the nuclear (200) peak, that in turn is an order of magnitude weaker than the main nuclear peaks. However, even such a weak peak at the incommensurate position should be clearly visible given CYCLOPS's resolution and sensitivity [29], since magnetic peaks as weak as 0.3% of the main nuclear peaks are routinely observed on

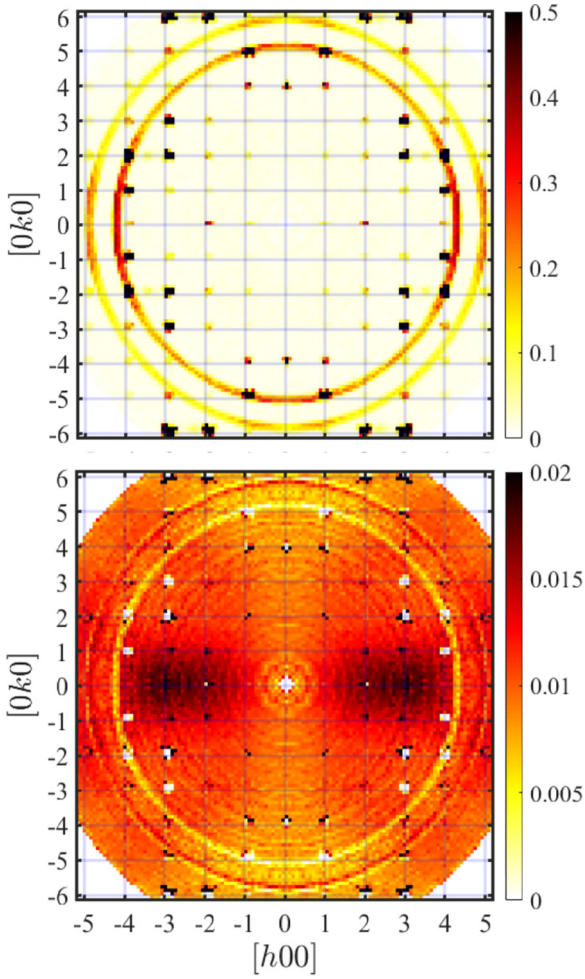

FIG. 9. Single-crystal neutron diffraction maps of the $(hk0)$ plane for $SrTb_2O_4$ measured on D7 at $T = 1.5$ K. The non-spin-flip (top panel) and spin-flip (bottom panel) channels are shown. To maximize the signal-to-noise ratio and average over statistics, the intensity map was symmetrized and subsequently unfolded.

the diffractometer as long as they have nonzero propagation vectors.

2. *Zero field polarized neutron diffraction*

A central claim of Ref. [20] regarding the magnetic ordering in $SrTb_2O_4$ is based on the observations made using the diffuse scattering spectrometer D7 with polarization analysis. Bragg peaks at $(\pm 1.6\ \pm 1\ 0)$ were reported in both SF and NSF channels with the polarization normal to the scattering plane [57]. We have also used the D7 instrument to test for magnetic correlations in a $SrTb_2O_4$ crystal. Figure 9 shows the intensity maps of the $(hk0)$ scattering plane for the SF and NSF channels at $T = 1.5$ K. The maps were recorded using a polarization direction along the vertical c axis, normal to the horizontal scattering plane.

The data show some powder rings due to the aluminium sample mount being imperfectly masked with cadmium; however, the diffuse background was dominated by forward scattering from windows and ambient neutrons which were correctly estimated from measuring the empty cryostat. The data in Fig. 9 have had this diffuse background estimate subtracted and have been symmetrized by combining data at equivalent $\{hkl\}$ before unfolding. Unsubtracted and presymmetrized data are shown in the Supplemental Material [24], Figs. S6 and S7.

Our measurements show no evidence for the incommensurate Bragg peaks reported at $(\pm 1.6\ \pm 1\ 0)$ in Ref. [20]. All the Bragg peaks observed in the NSF channel have integer h and k. They are due to nuclear scattering, and their intensities do not change much with temperature upon warming up to 50 K (the results of the measurements at selected higher temperatures are given in Fig. S7 in the Supplemental Material [24]). Note that, for the NSF map, the intensity scale (0 to 0.5 units) is chosen to emphasize the presence of any weaker peaks. The maximum intensities of the Bragg peaks shown on this map reaches about five units.

The intensity scale for the SF map is significantly lower, reflecting the fact that the diffuse scattering intensity is orders of magnitude lower compared to the Bragg peaks. The SF map also shows very small and localized features at the integer $(hk0)$ positions, some of which are negative. These are most probably due to a known issue in correcting for polarization inefficiency, stemming from using parameters determined from the diffuse scattering from amorphous quartz to correct sharp, intense, self-collimated Bragg scattering. These sharp features therefore cannot reliably be attributed to magnetic Bragg peaks from the sample.

The SF map in Fig. 9 shows substantial diffuse scattering which is clearly magnetic. The scattering is most intense around the $\langle 100 \rangle$ directions, particularly for $1.5 < h < 3.5$ and $|k| < 1$. Along the orthogonal $\langle 010 \rangle$ direction, the magnetic diffuse signal is clearly the weakest, while there is a visible intensity increase along the diagonal $\langle 110 \rangle$ directions.

The observed diffuse scattering in Fig. 9 is very different from that observed in Ref. [20] and also from those observed in the sister compounds $SrEr_2O_4$ and $SrHo_2O_4$ [3–5,58,59]. In $SrEr_2O_4$, the magnetic moments on the Er1 site form a $\mathbf{q} = 0$ structure clearly marked by the sharp magnetic peaks appearing below 0.75 K. At low temperatures, only a rather weak diffuse scattering is seen for this compound around the magnetic Bragg peaks; the intensity of the diffuse signal rapidly increases upon warming above 0.75 K and forms a characteristic lozenge pattern [4]. In $SrHo_2O_4$, because of the short-range nature of the ordering, the magnetic $\mathbf{q} = 0$ peaks remain broad even at the lowest temperature again forming the same pattern [5]. Figure 9 shows that such well-developed patterns of diffuse scattering are absent in our sample of $SrTb_2O_4$, where the diffuse scattering is much broader and not particularly structured. The diffuse scattering depicted in Fig. 1 of Ref. [20] for their sample of $SrTb_2O_4$ is also not centered around the $\mathbf{q} = 0$ positions and lacks the characteristic structure seen in $SrEr_2O_4$ and $SrHo_2O_4$.

The incident neutrons of $\lambda = 3.1$ Å used on D7 have an energy of 8.51 meV. As discussed in Sec. III B, the lower-energy crystal-field excitations in $SrTb_2O_4$ range from 0.71 to 2.22 meV [see Fig. 3(b)]. For these excitations, the quasistatic approximation works rather well. There is also a crystal-field level at 7.64 meV [see Fig. 3(a)] for which the integration over the spin-fluctuation spectrum will be incomplete, and it is possible that the entire paramagnetic signal was not

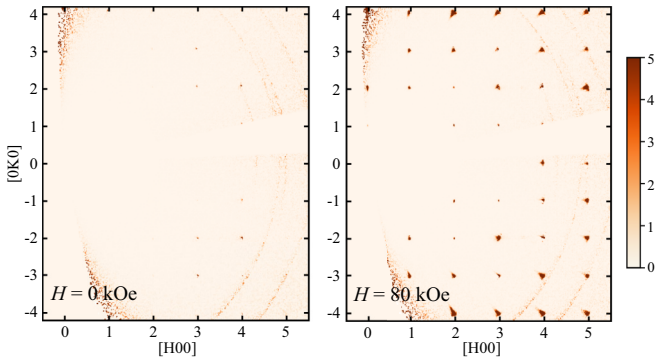

FIG. 10. Single-crystal neutron diffraction maps of the ($hk0$) plane for $SrTb_2O_4$ measured on WISH at $T = 35$ mK (left) in zero field and (right) in a field of 80 kOe, $H \parallel c$. The magnetic signal is isolated by subtracting a 10 K background.

observed within the given energy window. However, for the single-crystal measurements, a breakdown of the quasi-static approximation is typically seen as characteristic deformations of the diffuse scattering, resulting in a loss of symmetry when compared to the underlying lattice. As such deformations are not seen in the scattering maps depicted in Fig. 9, we therefore rule out a significant influence of the crystal-field effects on the magnetic diffuse scattering observed in $SrTb_2O_4$.

3. Neutron diffraction in applied field

The single-crystal neutron diffraction experiment on the WISH instrument was conducted with two objectives in mind.

Firstly, we wanted to extend the investigations down to dilution cryostat temperatures. On cooling down to $T = 35$ mK, the lowest experimentally available temperature, the intensity of all peaks remained practically unchanged and no new reflections were found in the ($hk0$) scattering plane, see Fig. 10, ruling out a magnetic ordering transition in zero field. This observation is further reinforced by the refinement of the extracted single-crystal intensities. Figure 11(b) shows the observed structure factors against the calculated ones for the nuclear structure refinement using the $Pnam.1'$ model for $SrTb_2O_4$. The agreement is quite satisfactory, also compared with the x-ray refinements reported in Table I, and the crystal parameters obtained and the reliability factors are reported in Table IV. Due to the limited number of reflections and the geometry constraints of the cryomagnet which allowed the collection in only the ($hk0$) plane, we refined isotropic atomic displacement parameters (ADPs) for all the atoms and constrained ADPs for all oxygen sites to the same value.

The second aim for the WISH experiment was to investigate the influence of applied field. The magnetic field was applied along the c axis at $T = 35$ mK, the measurements were taken in fields of 5, 10, 20, 40, and 80 kOe. We observed a significant increase in the intensity of most of the ($hk0$) peaks with integer h and k in the applied field. Figure 10 presents the background-subtracted intensity maps in zero field and in the maximum field of 80 kOe clearly showing an increase in the intensity of the $\mathbf{q} = 0$ peaks. Although the high-T background subtraction is not perfect (as for example, the powder lines from the sample holder are still visible after

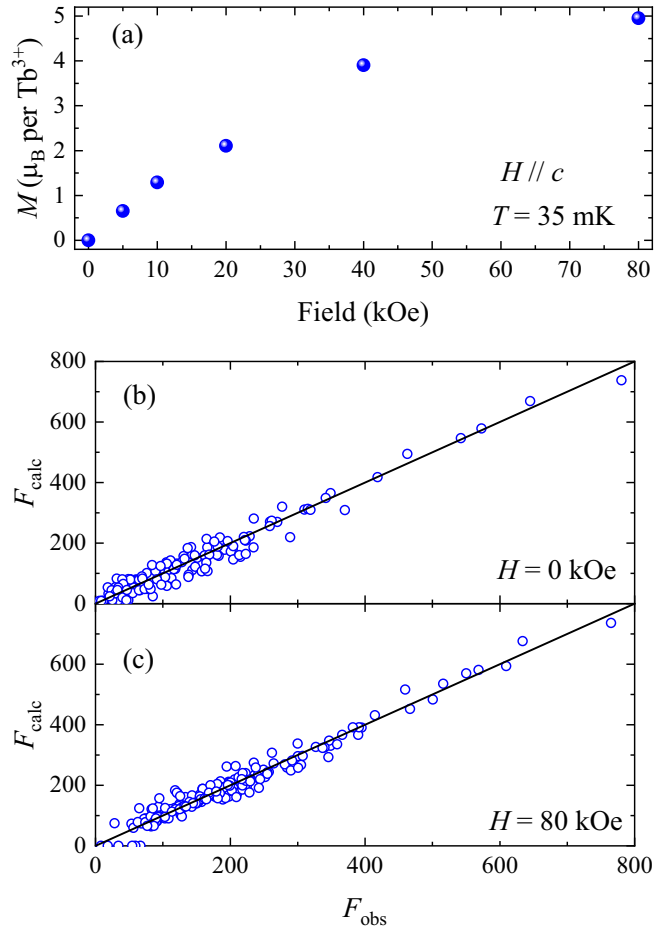

FIG. 11. (a) Evolution of the total magnetic moment per Tb^{3+} ion as observed by neutron diffraction at $T = 35$ mK. Observed structure factors versus calculated one for the single-crystal WISH data collected in (b) 0 kOe and (c) 80 kOe, the error-bars are smaller than the marker size.

subtraction), it is rather obvious that the field-induced magnetic intensity is orders of magnitude higher than any artifacts.

The data collected in 80 kOe were integrated and refined assuming a ferromagnetic structure with Tb moments aligned along the c direction. This corresponds to the magnetic space group $Pn'a'm$ derived from the $m\Gamma_4^+$ irreducible representation. The single-crystal refinement returned a good agreement between the observed and calculated structure factors as can be appreciated from Fig. 11(c). Atomic position, ADPs, and magnetic moments for the two Tb ions (constrained along the field direction) were refined and the results are reported in Table IV. The refinement converged with different magnetic moments values for the two Tb positions: $7.4(3)\mu_B$ and $2.5(2)\mu_B$ for Tb1 and Tb2, respectively. Attempts to constrain the two sites to have the same moment size or different moment ratios returned significantly worse fits. The predicted intensity maps look very similar for the models with only Tb1 or Tb2 having a magnetic moment on them, but rather different if both sites carry the same moment (see Fig. S8 in the Supplemental Material [24]).

The different moment size of the two RE sites is related to their different CEF environments, as observed in several other

TABLE IV. Crystal data, reliability factors, and structural parameters for the single-crystal refinements of the neutron diffraction data collected on WISH at 0 and 80 kOe. The atoms sit at the 4c Wyckoff position (x, y, 1/4).

Magnetic field	0 kOe	80 kOe
Space group	$Pnam.1'$	$Pn'a'm$
a, b, c (Å)	10.0(1), 12.9(1), 3.45(10)	
R_p	0.155	0.0899
R_{wp}	0.147	0.1043
# reflections	154	191
Sr x, y	0.749(1) 0.646(1)	0.750(1) 0.647(2)
Sr U_{iso} (Å^2)	0.014(6)	0.008(6)
O1 x, y	0.216(2) 0.178(2)	0.218(2) 0.175(2)
O2 x, y	0.130(2) 0.483(1)	0.128(2) 0.482(2)
O3 x, y	0.514(1) 0.781(1)	0.510(2) 0.781(2)
O4 x, y	0.430(1) 0.421(1)	0.427(2) 0.421(2)
O1,2,3,4 U_{iso} (Å^2)	0.020(5)	0.014(4)
Tb1 x, y	0.426(1) 0.115(1)	0.425(1) 0.113(1)
Tb1 U_{iso} (Å^2)	0.014(5)	0.011(3)
Tb1 $M_z(\mu_B)$	0	7.4(3)
Tb2 x, y	0.418(1) 0.612(1)	0.418(1) 0.611(1)
Tb2 U_{iso} (Å^2)	0.012(5)	0.011(3)
Tb2 $M_z(\mu_B)$	0	2.5(2)

$SrRE_2O_4$ compounds [12,17,18]. This is also fully consistent with our calculations based on the crystal-field parameters shown in Tables II, which returned very different sizes for the Tb1 and Tb2 moments in 80 kOe of magnetic field applied along the c axis.

The observed total ferromagnetic moment as function of applied field [see Fig. 11(a)] is consistent with the magnetization data shown in Fig. 6 despite having been taken at different temperatures, 35 mK and 1.5 K, respectively. This is not surprising, as for $H \parallel c$, the magnetization in 80 kOe reaches saturation and therefore is practically temperature independent for $T < 10$ K.

IV. SUMMARY

To summarize, we have shown that $SrTb_2O_4$ does not order magnetically down to at least 35 mK. Various results from neutron diffraction, magnetic susceptibility, and heat capacity measurements definitively rule out a transition at 4.28 K contrary to previous reports. The nonmagnetic ground state of $SrTb_2O_4$ is governed by an intricate balance of the geometrically frustrated exchange interactions between the Tb^{3+} ions and the splitting of the energy levels by the crystal fields acting on them.

Using a constrained search procedure, we were able to obtain a set of crystal-field parameters consistent with previous work on other $SrRE_2O_4$ systems and which also qualitatively agrees with the measured susceptibility and magnetization (predicting that the c axis is the easy axis and the a axis is the hard axis), and which also agrees with the ordered moments of the two Tb sites as determined by neutron diffraction. However, we should note that due to the large number of symmetry allowed crystal-field parameters, the fitting problem is quite unconstrained, and that the parameters we obtained may not necessarily be the correct values.

ACKNOWLEDGMENTS

We are grateful to B. Fåk and B. Z. Malkin for discussions, as well as to D. L. Quintero-Castro for sharing unpublished data. The authors would like to acknowledge the contributions of D. L. Elmer and M. J. J. Johnson to the preparation of $SrTb_2O_4$ polycrystalline and crystal samples through their participation in the undergraduate project. We would also like to acknowledge the expertise and dedication of the low-temperature groups at both the Institut Laue-Langevin and ISIS. The work at the University of Warwick was supported by EPSRC through grants EP/M028771/1 and EP/T005963/1.

DATA AVAILABILITY

All data underlying this work are available from the authors upon reasonable request.

[1] H. Karunadasa, Q. Huang, B. G. Ueland, J. W. Lynn, P. Schiffer, K. A. Regan, and R. J. Cava, Honeycombs of triangles and magnetic frustration in SrL_2O_4 (L = Gd, Dy, Ho, Er, Tm, and Yb), Phys. Rev. B **71**, 144414 (2005).

[2] A. Fennell, V. Y. Pomjakushin, A. Uldry, B. Delley, B. Prévost, A. Désilets-Benoit, A. D. Bianchi, R. I. Bewley, B. R. Hansen, T. Klimczuk, R. J. Cava, and M. Kenzelmann, Evidence for $SrHo_2O_4$ and $SrDy_2O_4$ as model J_1-J_2 zigzag chain materials, Phys. Rev. B **89**, 224511 (2014).

[3] J.-J. Wen, W. Tian, V. O. Garlea, S. M. Koohpayeh, T. M. McQueen, H.-F. Li, J.-Q. Yan, J. A. Rodriguez-Rivera, D. Vaknin, and C. L. Broholm, Disorder from order among anisotropic next-nearest-neighbor Ising spin chains in $SrHo_2O_4$, Phys. Rev. B **91**, 054424 (2015).

[4] T. J. Hayes, G. Balakrishnan, P. P. Deen, P. Manuel, L. C. Chapon, and O. A. Petrenko, Coexistence of the long-range and short-range magnetic order components in $SrEr_2O_4$, Phys. Rev. B **84**, 174435 (2011).

[5] O. Young, A. R. Wildes, P. Manuel, B. Ouladdiaf, D. D. Khalyavin, G. Balakrishnan, and O. A. Petrenko, Highly frustrated magnetism in $SrHo_2O_4$: Coexistence of two types of short-range order, Phys. Rev. B **88**, 024411 (2013).

[6] C. Bidaud, O. Simard, G. Quirion, B. Prévost, S. Daneau, A. D. Bianchi, H. A. Dabkowska, and J. A. Quilliam, Dimensionality and irreversibility of field-induced transitions in $SrDy_2O_4$, Phys. Rev. B **93**, 060404(R) (2016).

[7] N. Qureshi, O. Fabelo, P. Manuel, D. D. Khalyavin, E. Lhotel, S. Riberolles, G. Balakrishnan, and O. A. Petrenko, Field-induced magnetic states in geometrically frustrated $SrEr_2O_4$, SciPost Phys. **11**, 007 (2021).

[8] J. S. Gardner, S. R. Dunsiger, B. D. Gaulin, M. J. P. Gingras, J. E. Greedan, R. F. Kiefl, M. D. Lumsden, W. A. MacFarlane, N. P. Raju, J. E. Sonier, I. Swainson, and Z. Tun, Cooperative paramagnetism in the geometrically frustrated pyrochlore antiferromagnet $Tb_2Ti_2O_7$, Phys. Rev. Lett. **82**, 1012 (1999).

[9] M. J. P. Gingras, B. C. den Hertog, M. Faucher, J. S. Gardner, S. R. Dunsiger, L. J. Chang, B. D. Gaulin, N. P. Raju, and J. E. Greedan, Thermodynamic and single-ion properties of Tb^{3+} within the collective paramagnetic-spin liquid state of the frustrated pyrochlore antiferromagnet $Tb_2Ti_2O_7$, Phys. Rev. B **62**, 6496 (2000).

[10] M. Ruminy, S. Guitteny, J. Robert, L.-P. Regnault, M. Boehm, P. Steffens, H. Mutka, J. Ollivier, U. Stuhr, J. S. White, B. Roessli, L. Bovo, C. Decorse, M. K. Haas, R. J. Cava, I. Mirebeau, M. Kenzelmann, S. Petit, and T. Fennell, Magnetoelastic excitation spectrum in the rare-earth pyrochlore $Tb_2Ti_2O_7$, Phys. Rev. B **99**, 224431 (2019).

[11] D. Slobinsky, L. Pili, G. Baglietto, S. A. Grigera, and R. A. Borzi, Monopole matter from magnetoelastic coupling in the Ising pyrochlore, Commun. Phys. **4**, 56 (2021).

[12] O. A. Petrenko, G. Balakrishnan, N. R. Wilson, S. de Brion, E. Suard, and L. C. Chapon, Low-temperature magnetic ordering in $SrEr_2O_4$, Phys. Rev. B **78**, 184410 (2008).

[13] O. A. Petrenko, O. Young, D. Brunt, G. Balakrishnan, P. Manuel, D. D. Khalyavin, and C. Ritter, Evolution of spin correlations in $SrDy_2O_4$ in an applied magnetic field, Phys. Rev. B **95**, 104442 (2017).

[14] N. Gauthier, B. Prevost, A. Amato, C. Baines, V. Pomjakushin, A. D. Bianchi, R. J. Cava, and M. Kenzelmann, Evidence for spin liquid ground state in $SrDy_2O_4$ frustrated magnet probed by μSR, J. Phys.: Conf. Ser. **828**, 012014 (2017).

[15] N. Gauthier, A. Fennell, B. Prévost, A.-C. Uldry, B. Delley, R. Sibille, A. Désilets-Benoit, H. A. Dabkowska, G. J. Nilsen, L.-P. Regnault, J. S. White, C. Niedermayer, V. Pomjakushin, A. D. Bianchi, and M. Kenzelmann, Absence of long-range order in the frustrated magnet $SrDy_2O_4$ due to trapped defects from a dimensionality crossover, Phys. Rev. B **95**, 134430 (2017).

[16] D. L. Quintero-Castro, B. Lake, M. Reehuis, A. Niazi, H. Ryll, A. T. M. N. Islam, T. Fennell, S. A. J. Kimber, B. Klemke, J. Ollivier, V. G. Sakai, P. P. Deen, and H. Mutka, Coexistence of long- and short-range magnetic order in the frustrated magnet $SrYb_2O_4$, Phys. Rev. B **86**, 064203 (2012).

[17] N. Qureshi, A. R. Wildes, C. Ritter, B. Fåk, S. X. M. Riberolles, M. Ciomaga Hatnean, and O. A. Petrenko, Magnetic structure and low-temperature properties of geometrically frustrated $SrNd_2O_4$, Phys. Rev. B **103**, 134433 (2021).

[18] N. Qureshi, B. Z. Malkin, S. X. M. Riberolles, C. Ritter, B. Ouladdiaf, G. Balakrishnan, M. Ciomaga Hatnean, and O. A. Petrenko, Magnetic structures of geometrically frustrated $SrGd_2O_4$ derived from powder and single-crystal neutron diffraction, Phys. Rev. B **105**, 014425 (2022).

[19] Y. I. Dublenych and O. A. Petrenko, An Ising model on a 3D honeycomb zigzag-ladder lattice: A solution to the ground-state problem, SciPost Phys. Core **5**, 047 (2022).

[20] H. Li, C. Zhang, A. Senyshyn, A. Wildes, K. Schmalzl, W. Schmidt, M. Boehm, E. Ressouche, B. Hou, P. Meuffels, G. Roth, and T. Bruckel, Incommensurate antiferromagnetic order in the manifoldly-frustrated $SrTb_2O_4$ with transition temperature up to 4.28 K, Front. Phys. **2**, 42 (2014).

[21] B. Prévost, N. Gauthier, V. Y. Pomjakushin, B. Delley, H. C. Walker, M. Kenzelmann, and A. D. Bianchi, Coexistence of magnetic fluctuations and long-range order in the one-dimensional J_1-J_2 zigzag chain materials $BaDy_2O_4$ and $BaHo_2O_4$, Phys. Rev. B **98**, 144428 (2018).

[22] Y. Doi, W. Nakamori, and Y. Hinatsu, Crystal structures and magnetic properties of magnetically frustrated systems $BaLn_2O_4$ and $Ba_3Ln_4O_9$ (Ln = lanthanide), J. Phys.: Condens. Matter **18**, 333 (2006).

[23] A. A. Aczel, L. Li, V. O. Garlea, J.-Q. Yan, F. Weickert, V. S. Zapf, R. Movshovich, M. Jaime, P. J. Baker, V. Keppens, and D. Mandrus, Spin-liquid ground state in the frustrated J_1-J_2 zigzag chain system $BaTb_2O_4$, Phys. Rev. B **92**, 041110(R) (2015).

[24] See Supplemental Material at http://link.aps.org/supplemental/10.1103/PhysRevB.111.054415 for additional details on sample preparations and CEF analysis, as well as additional data on magnetization and neutron diffraction measurements. The Supplemental Material also contains the cif file with the refined crystal structure parameters and Refs. [44,46,60].

[25] Rigaku Oxford Diffraction, *CrysAlis PRO* (Oxford Diffraction Ltd., Yarnton, UK, 2019).

[26] G. M. Sheldrick, SHELXT–Integrated space-group and crystal-structure determination, Acta. Crystallogr. Sect. A **71**, 3 (2015).

[27] G. M. Sheldrick, Crystal structure refinement with SHELXT, Acta. Crystallogr. Sect. C **71**, 3 (2015).

[28] O. V. Dolomanov, L. J. Bourhis, R. J. Gildea, J. A. K. Howard, and H. Puschmann, OLEX2: a complete structure solution, refinement and analysis program, J. Appl. Cryst. **42**, 339 (2009).

[29] B. Ouladdiaf, J. Archer, J. R. Allibon, P. Decarpentrie, M.-H. Lemée-Cailleau, J. Rodríguez-Carvajal, A. W. Hewat, S. York, D. Brau, and G. J. McIntyre, CYCLOPS - a reciprocal-space explorer based on CCD neutron detectors, J. Appl. Cryst. **44**, 392 (2011).

[30] J. R. Stewart, P. P. Deen, K. H. Andersen, H. Schober, J.-F. Barthélémy, J. M. Hillier, A. P. Murani, T. Hayes, and B. Lindenau, Disordered materials studied using neutron polarization analysis on the multi-detector spectrometer, D7, J. Appl. Cryst. **42**, 69 (2009).

[31] L. C. Chapon, P. Manuel, P. G. Radaelli, C. Benson, L. Perrott, S. Ansell, N. J. Rhodes, D. Raspino, D. Duxbury, E. Spill, and J. Norris, Wish: the new powder and single crystal magnetic diffractometer on the second target station, Neutron News **22**, 22 (2011).

[32] O. Petrenko *et al.*, Magnetic Ordering in $SrTb_2O_4$ (2008), https://doi.org/10.5291/ILL-DATA.DIR-162.

[33] O. Petrenko *et al.*, Low-temperature magnetic correlations in $SrTb_2O_4$ (2019), https://doi.org/10.5286/ISIS.E.RB1920479.

[34] O. Arnold, J. Bilheux, J. Borreguero, A. Buts, S. Campbell, L. Chapon, M. Doucet, N. Draper, R. F. Leal, M. Gigg, V. Lynch, A. Markvardsen, D. Mikkelson, R. Mikkelson, R. Miller, K. Palmen, P. Parker, G. Passos, T. Perring, P. Peterson, S. Ren, M. Reuter, A. Savici, J. Taylor, R. Taylor, R. Tolchenov, W. Zhou, and J. Zikovsky, Mantid—data analysis and visualization package for neutron scattering and μSR experiments, Nucl. Instrum. Meth. A **764**, 156 (2014).

[35] V. Petříček, M. Dušek, and L. Palatinus, Crystallographic computing system JANA2006: general features, Z. Krist.-Cryst. Mater. **229**, 345 (2014).

[36] B. J. Campbell, H. T. Stokes, D. E. Tanner, and D. M. Hatch, ISODISPLACE: A web-based tool for exploring structural distortions, J. Appl. Crystallogr. **39**, 607 (2006).

[37] R. I. Bewley, T. Guidi, and S. Bennington, MERLIN: a high count rate chopper spectrometer at isis, Notiziario Neutroni e Luce di Sincrotrone **14**, 22 (2009).

[38] O. Petrenko *et al.*, Low-temperature magnetic correlations in $SrTb_2O_4$ (2019), https://doi.org/10.5286/ISIS.E.RB1910416-1.

[39] Y.-L. Wang and B. R. Cooper, Collective excitations and magnetic ordering in materials with singlet crystal-field ground state, Phys. Rev. **172**, 539 (1968).

[40] J. Jensen and A. R. Mackintosh, *Rare Earth Magnetism* (Clarendon Press Oxford, England, 1991).

[41] A. Bhat Kademane, D. Quintero-Castro, K. Siemensmeyer, C. Salazar-Mejia, D. Gorbunov, J. Stewart, H. Luetkens, C. Baines, and H. Li, Crystal field effects in the zig-zag chain compound $SrTm_2O_4$, J. Magn. Magn. Mater. **551**, 169020 (2022).

[42] M. D. Le, K. A. McEwen, M. Rotter, J. Jensen, R. I. Bewley, T. Guidi, and D. Fort, Dispersive crystal field excitations and quadrupolar interactions in UPd_3, J. Phys.: Condens. Matter **24**, 036002 (2012).

[43] D. J. Newman and B. Ng, `QBASIC` programs, in *Crystal Field Handbook* (Cambridge University Press, England, 2000), pp. 239–253.

[44] B. Z. Malkin, S. I. Nikitin, I. E. Mumdzhi, D. G. Zverev, R. V. Yusupov, I. F. Gilmutdinov, R. Batulin, B. F. Gabbasov, A. G. Kiiamov, D. T. Adroja, O. Young, and O. A. Petrenko, Magnetic and spectral properties of the multisublattice oxides SrY_2O_4:Er^{3+} and $SrEr_2O_4$, Phys. Rev. B **92**, 094415 (2015).

[45] B. Z. Malkin and S. I. Nikitin (private communication).

[46] B. Z. Malkin, R. V. Yusupov, I. F. Gilmutdinov, R. G. Batulin, A. G. Kiiamov, B. F. Gabbasov, S. I. Nikitin, and B. Barbara, Double-loop hysteresis of multisite dilute $Sr(Y_{1-x}Dy_x)_2O_4$ single crystal Kramers paramagnets: Electron-phonon interaction, quantum tunneling, and cross relaxation, Phys. Rev. B **109**, 054434 (2024).

[47] P. Virtanen, R. Gommers, T. E. Oliphant, M. Haberland, T. Reddy, D. Cournapeau, E. Burovski, P. Peterson, W. Weckesser, J. Bright, S. J. van der Walt, M. Brett, J. Wilson, K. J. Millman, N. Mayorov, A. R. J. Nelson, E. Jones, R. Kern, E. Larson, C. J. Carey, İ. Polat, Y. Feng, E. W. Moore, J. VanderPlas, D. Laxalde, J. Perktold, R. Cimrman, I. Henriksen, E. A. Quintero, C. R. Harris, A. M. Archibald, A. H. Ribeiro, F. Pedregosa, P. van Mulbregt, and SciPy 1.0 Contributors, SciPy 1.0: fundamental algorithms for scientific computing in python, Nat. Methods **17**, 261 (2020).

[48] Mantid Project, Mantid version 6.8 (2023), `http://doi.org/10.5286/SOFTWARE/MANTID6.8`.

[49] M. D. Le, CEF fitting programs for $SrTb_2O_4$ (2023), `https://github.com/mducle/srtb2o4-cef`.

[50] P. Fabi, Appendix, in *FOCUS Program Manual* (The Central Laboratory for the Research Councils, England, 1995), pp. 59–60.

[51] M. Rotter, High speed algorithm for the calculation of magnetic and orbital excitations in rare earth based systems, Comput. Mater. Sci. **38**, 400 (2006).

[52] S. Wu, Y. Zhu, H. Gao, Y. Xiao, J. Xia, P. Zhou, D. Ouyang, Z. Li, Z. Chen, Z. Tang, and H.-F. Li, Supernecking crystal growth and structural and magnetic properties of $SrTb_2O_4$ single crystals, ACS Omega **5**, 16584 (2020).

[53] D. L. Quintero-Castro (private communication).

[54] T. J. Hayes, O. Young, G. Balakrishnan, and O. A. Petrenko, Magnetisation studies of geometrically frustrated antiferromagnets $SrLn_2O_4$, with Ln = Er, Dy, and Ho, J. Phys. Soc. Jpn. **81**, 024708 (2012).

[55] N. Gauthier, A. Fennell, B. Prévost, A. Désilets-Benoit, H. A. Dabkowska, O. Zaharko, M. Frontzek, R. Sibille, A. D. Bianchi, and M. Kenzelmann, Field dependence of the magnetic correlations of the frustrated magnet $SrDy_2O_4$, Phys. Rev. B **95**, 184436 (2017).

[56] O. Petrenko *et al.*, Experiment on CYCLOPS (2018), https://doi.ill.fr/10.5291/ILL-DATA.EASY-300.

[57] We note that the Bragg peaks at the ($\pm$1.6$\pm$10) positions do not follow fourfold symmetry as claimed in Ref. [20].

[58] S. Ghosh, H. D. Zhou, L. Balicas, S. Hill, J. S. Gardner, Y. Qiu, and C. R. Wiebe, Short range ordering in the modified honeycomb lattice compound $SrHo_2O_4$, J. Phys.: Condens. Matter **23**, 164203 (2011).

[59] O. Young, G. Balakrishnan, P. Manuel, D. Khalyavin, A. Wildes, and O. A. Petrenko, Field-induced transitions in highly frustrated $SrHo_2O_4$, Crystals **9**, 488 (2019).

[60] S. I. Nikitin, E. M. Kutasheva, R. V. Yusupov, R. G. Batullin, A. G. Kiiamov, I. E. Mumdzhi, and B. Z. Malkin, Selective laser spectroscopy of impurity Ho^{3+} centers in SrY_2O_4 single crystal, Opt. Spectrosc. **131**, 441 (2023).